minerals

MDPI

Article

Geochronological and Paleomagnetic Constraints on the Lower Cretaceous Dalazi Formation from the Yanji Basin, NE China, and its Tectonic Implication

Zhongshan Shen [1,2,3], Zhiqiang Yu [4,5,*], Hanqing Ye [1,2,3], Zuohuan Qin [6] and Dangpeng Xi [6]

1 State Key Laboratory of Lithospheric Evolution, Institute of Geology and Geophysics, Chinese Academy of Sciences, Beijing 100029, China; zsshen@mail.iggcas.ac.cn (Z.S.); yehq@mail.iggcas.ac.cn (H.Y.)
2 College of Earth and Planetary Sciences, University of Chinese Academy of Sciences, Beijing 100049, China
3 Innovation Academy for Earth Science, Chinese Academy of Sciences, Beijing 100029, China
4 Key Laboratory of Vertebrate Evolution and Human Origin of Chinese Academy of Sciences, Institute of Vertebrate Paleontology and Paleoanthropology, Chinese Academy of Sciences, Beijing 100044, China
5 CAS Centre for Excellence in Life and Paleoenvironment, Beijing 100044, China
6 State Key Laboratory of Biogeology and Environmental Geology, China University of Geosciences, Beijing 100083, China; qinzh@cugb.edu.cn (Z.Q.); xidp@cugb.edu.cn (D.X.)
* Correspondence: zhiqiangyu@mail.iggcas.ac.cn

Abstract: The Lower Cretaceous Dalazi Formation in the Yanji Basin, eastern Jilin Province is of particular interest because it contains key fresh water fossil taxa, oil and gas resources, a potential terrestrial Albian–Cenomanian boundary, and regional unconformities. However, the lack of a precise chronology for the non-marine strata has precluded a better understanding of the regional stratigraphic correlation and terrestrial processes. Here, we report magnetostratigraphic and U–Pb geochronologic results of a sedimentary sequence from the Xing'antun section in the Yanji Basin. Thirty-two zircons from the tuff sample were analyzed by secondary ion mass spectrometry (SIMS); the U–Pb zircon dating method yielded a weighted mean of $^{206}Pb/^{238}U$ age of 105.7 ± 0.8 Ma (2σ, internal error). Paleomagnetic results show that the Dalazi Formation is of normal polarity, which was correlated to the early chron C34n constrained by the SIMS U–Pb zircon geochronologic data, further demonstrating that the terrestrial sedimentary sequence of the upper Dalazi Formation is of late Albian age. The established geochronologic framework allows the regional correlation of the Dalazi Formation in the Yanji Basin to the strata from other terrestrial sequences in northeastern China. The similar geodynamic and geologic background between the Yanji Basin and other terrestrial rift basins in northeastern China suggests that the unconformity between the Dalazi and Longjing formations may represent syn-rift and post-rift stages in the Yanji Basin, and thus the switch from extension to contraction during the mid-Cretaceous, precisely constrained to ~106–101 Ma based on our new chronology and previously published high-precision U–Pb dating of the lower Longjing Formation. It is most likely attributable to the docking of the west Pacific plate along the East Asian continental margin.

Keywords: Early Cretaceous; Dalazi Formation; SIMS U–Pb geochronology; magnetostratigraphy

Citation: Shen, Z.; Yu, Z.; Ye, H.; Qin, Z.; Xi, D. Geochronological and Paleomagnetic Constraints on the Lower Cretaceous Dalazi Formation from the Yanji Basin, NE China, and its Tectonic Implication. *Minerals* **2021**, *11*, 527. https://doi.org/10.3390/min11050527

Academic Editors: Sung Won Kim and Seong-Jun Cho

Received: 17 April 2021
Accepted: 13 May 2021
Published: 17 May 2021

1. Introduction

Cretaceous non-marine strata in northern China have attracted wide attention from geologists and paleontologists because they contain a large number of exceptionally preserved fresh-water vertebrates (the Early Cretaceous Jehol Biota) [1,2], a nearly complete terrestrial Cretaceous record [3–8], a series of geodynamic (e.g., [9]) and paleoenvironmental events [10,11]. Comprehensive research in the Songliao, Hailaer, and Dasanjiang basins [12,13] in northeastern China, and in the Jiaolai Basin in northern China [14,15] has advanced our knowledge of the evolutionary process of the continental rift basin and the terrestrial climatic changes. These data provide crucial evidence that the integration of marine and terrestrial records and how terrestrial systems respond to both regional- and global-scale environmental changes. Additionally, they provide a rare opportunity to study the sedimentary records of the terrestrial mid-Cretaceous (Albian–Cenomanian) [16,17] because of marine transgressions in the world during this time [18,19].

The Yanji Basin is a typical continental rift basin in eastern Jilin Province (Figure 1) that is of particular significance due to its terrestrial biota, oil and gas resources, and nearly complete Early Cretaceous strata. The biota from the Dalazi Formation in the Yanji Basin and its adjacent areas comprises abundant fossil terrestrial and freshwater invertebrates such as bivalves, ostracods, and clam shrimp, along with vertebrates such as fish and lizard, and diverse fossil flora (e.g., [20–28]. The fossils have significantly advanced our understanding of the evolution of terrestrial flora, as it documents a transition from Early Cretaceous fern gymnosperm flora to Late Cretaceous angiosperm flora [29].

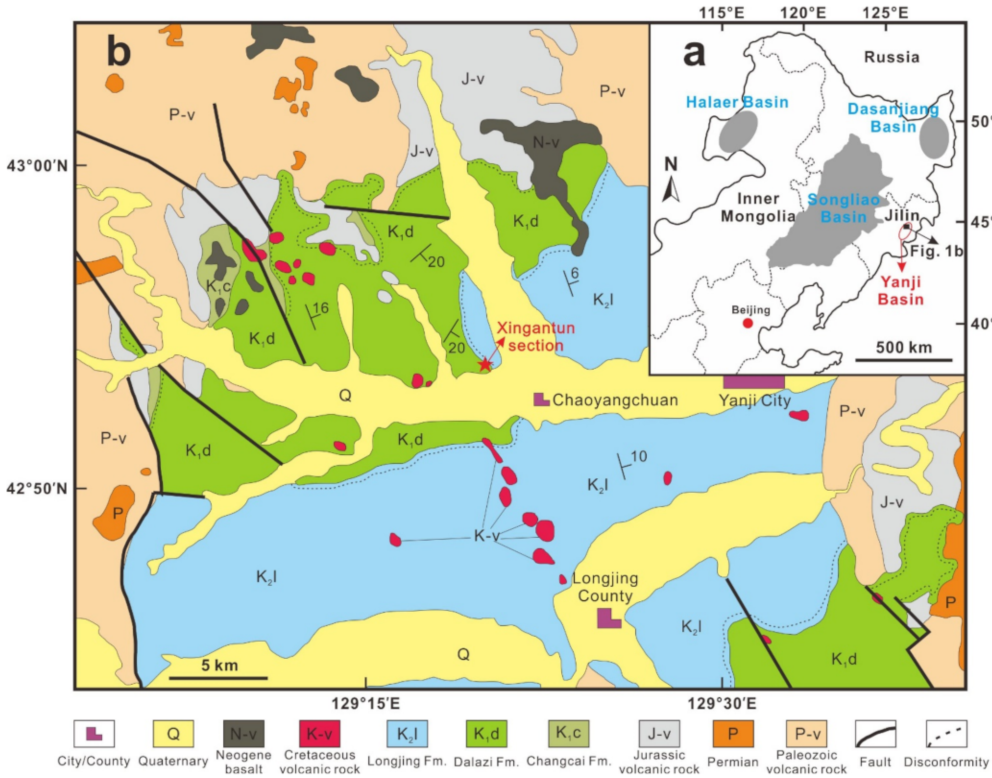

Figure 1. Schematic regional geology of northeastern China (**a**) and the Yanji Basin and the location of the Xing'antun section (red star) (**b**). Geological map modified from the 1: 250,000 geologic map of the Yanji area.

Regional unconformity between the Dalazi and Longjing formations was identified through seismic, geologic and logging data, which may represent the syn-rift and post-rift stages in the Yanji Basin [30]. The terrestrial volcanic-sedimentary basins in northeastern Asia record this stratigraphic unconformity during the mid-Cretaceous, such as the Songliao Basin, the Dasanjiang Basin, and the Hailaer Basin [13,31]. However, the precise age constraint on the unconformity in the Yanji Basin and its stratigraphic correlation to other terrestrial rift basins in northeastern China remains unclear due to the lack of a precise chronologic framework, which prevents our understanding of the tectonic evolution during this time.

The precise geologic age of the Dalazi Formation is still debatable, despite the fact that it was regarded as Early Cretaceous and Late Cretaceous based on biostratigraphy and radiometric dates (e.g., [26,32,33]). The age bracket of the Dalazi Formation is around 109.9–

96.2 Ma based on different dating methods, such as U–Pb zircon dating [26,32–35] (Figure 2), biostratigraphy [25,36], and thermochronology [37]. Most recently, Zhong et al. [26] reported a weighted mean secondary ion mass spectrometry (SIMS) U–Pb zircon age of 105.1 ± 0.4 Ma for the uppermost of the Dalazi Formation. The lack of precise age for the formation has precluded our understanding of the evolutionary history of this basin and its regional stratigraphic correlation. In this study, we report the results of magnetostratigraphic and SIMS U–Pb zircon dating of the Xing'antun section in the Yanji Basin. These data provide stringent age controls on the Cretaceous terrestrial fauna and flora and associated structural activity in the Yanji Basin.

2. Geologic Setting and Sampling

The Yanji Basin is located in eastern Jilin Province, northeast China (Figure 1). The basement of the Yanji Basin consists of Paleozoic granite [10,27,38] (Figure 1) on which the Cretaceous sedimentary sequences rest unconformably. The Cretaceous strata in the Yanji Basin consist of six lithologic formations, from oldest to youngest including Tuntianying, Changcai, Quanshuicun, Tongfosi, Dalazi, and Longjing formations (e.g., [33,39–41]).

Based on seismic, geologic and logging data, three regional unconformities separate the basin fill into three tectonostratigraphic sequences: the pre-rift stage includes the Tuntianying Formation, the syn-rift stage includes the Changcai, Quanshuicun, Tongfosi and Dalazi formations, and the post-rift stage includes the Longjing Formation [30] (Figure 2).

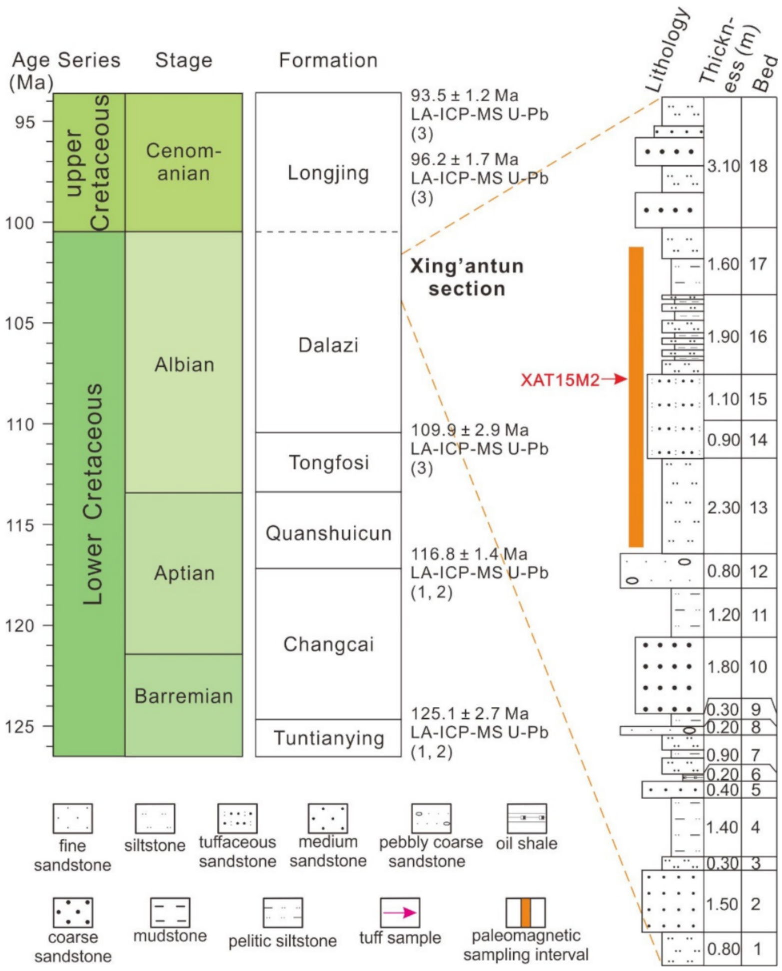

Figure 2. Chronostratigraphy of the Cretaceous strata in the Yanji Basin and the positions of the tuff sample and paleomagnetic samples. The international chronostratigraphic chart of the Cretaceous was after [42]. References: (1): [32]; (2): [33]; (3): [34].

The Tuntianying and Quanshuicun formations are mainly composed of andesites and volcaniclastic rocks. The Changcai Formation is coal-bearing and contains abundant plant fossils [33]. The Tongfosi and Dalazi formations consist of the most important hydrocarbon source rocks within the Yanji Basin. Vertebrate fossils, e.g., dinosaurs and crocodiles are preserved in the Longjing Formation [43].

3. Sampling and Analytical Methods

3.1. Sampling

The Dalazi Formation crops out in both Longjing County within the Yanji Basin and Wangqing County. The Xing'antun section (43.89° N, 129.34° E) investigated in this study lies in the eastern part of the Yanji Basin, eastern Jilin Province, northeastern China. Preliminary lithostratigraphic, biostratigraphic, and geologic investigations show that the entire Xing'antun section can be assigned to the upper part of the Dalazi Formation (Figure 1). For details of the lithology, readers are referred to the relevant lithological description in Table 1. In 2015, a tuff sample (XAT15M2) was collected from this section for SIMS U–Pb dating (Figures 1 and 2). Thin section studies show that this sample is composed of slightly altered feldspar, quartz, altered biotite, and accessory minerals such as zircon (Figure S1). The lithology characteristics support a volcanic pyroclastic origin. In this instance, the age defined by zircons would be the depositional age of the tuff bed.

Later, oriented paleomagnetic samples were collected using a gasoline-powered drill from this outcrop section, 28 tuff and tuffaceous siltstone layers were taken at ~30–40 cm intervals, from the tuff beds of the upper part of the Dalazi Formation (Figure 2). All the core samples were oriented with a magnetic compass and sun compass; then, they were cut into standard specimens with a length of 2 cm and diameter of 2.54 cm in the laboratory for paleomagnetic analysis.

3.2. Rock Magnetic Measurements

Rock magnetic measurements include the temperature dependence of magnetic susceptibility (χ–T curves), hysteresis loops, isothermal remanent magnetization (IRM) acquisition and its back-field demagnetization of the saturation IRM (SIRM), first order reversal curves (FORCs), and IRM component analysis (Figure 3, Figure 4 and Figure 5).

χ–T curves were measured using a MFK1-FA Kappabridge with a CS-3 high-temperature furnace (AGICO, Brno, Czech Republic) in an argon atmosphere heated from room temperature up to 700 °C and cooled back to room temperature. The susceptibility values were obtained by subtracting the empty furnace using the CUREVAL 8.0 program (AGICO, Brno, Czech Republic).

Hysteresis loops, IRM, and FORCs were measured on a MicroMag 3900 Vibrating Sample Magnetometer (VSM) (Princeton Measurements Corp., Princeton, NJ, USA) at room temperature. For each sample the magnetic field was cycled with a maximum field of 1 T, but are cut off at 0.5 T for clarity when plotting. The hysteresis parameters saturation magnetization (Ms), saturation remanence (Mrs), and coercivity (Bc) were calculated after subtracting the paramagnetic contributions. The SIRM was then demagnetized in a stepwise backfield up to −500 mT to obtain the coercivity of remanence (Bcr). Ms, Mrs, Bc and Bcr were determined, and their ratios were combined in a Day plot [44]. The S-ratio is defined as the ratio of isothermal remnant magnetization acquired at −0.3 T ($IRM_{-0.3\,T}$) to the saturation IRM acquired at 1 T (IRM_{1T}, hereinafter termed SIRM). IRM component analysis is based on cumulative log Gaussian analysis [45–47].

Table 1. Lithology of the Xing'antun section.

Layers	Lithological Descriptions	Thickness/m
1.	Yellow thick-bedded medium-fine grained sandstones.	0.8
2.	Gray green thin-bedded medium-fine grained sandstones.	1.5
3.	Grayish green medium-thick bedded medium grained sandstone.	0.3
4.	Light gray green thin-bedded argillaceous siltstones.	1.4
5.	Light gray green thick-bedded medium fine sandstones at the bottom, changes to light gray green thin-bedded fine sandstone upward.	0.4
6.	Dark grayish green and grayish black thin-bedded silty shales (oil shales).	0.2
7.	Yellow thick-bedded siltstones, intercalated with gray black thin-bedded silty mudstones.	0.9
8.	Yellow thick-bedded gravelly coarse sandstones.	0.2
9.	Purplish red medium-thin bedded silty mudstones.	0.3
10.	Yellow thick-bedded medium-coarse grained sandstones.	1.8
11.	Variegated (grayish green, dark purple) thin-bedded silty mudstones, intercalated with calcareous nodules.	1.2
12.	Yellow thick-bedded medium-coarse gravelly sandstones.	0.8
13.	Grayish green medium-thin bedded siltstones.	2.3
14.	Dark and brown thin-bedded siltstone (tuffaceous siltstone?), yields plant rhizome fossils.	0.9
15.	Light red thin-bedded tuffs, containing impurities (silty). Poor consolidation and scattered.	1.1
16.	Light gray green thick-bedded tuffs, show good consolidation.	1.9
17.	Gray green thick-bedded siltstones, interbedded with gray green thin-bedded argillaceous siltstones.	1.6
18.	of Yellow thin-bedded siltstones, interbedded with sandstones.	3.1

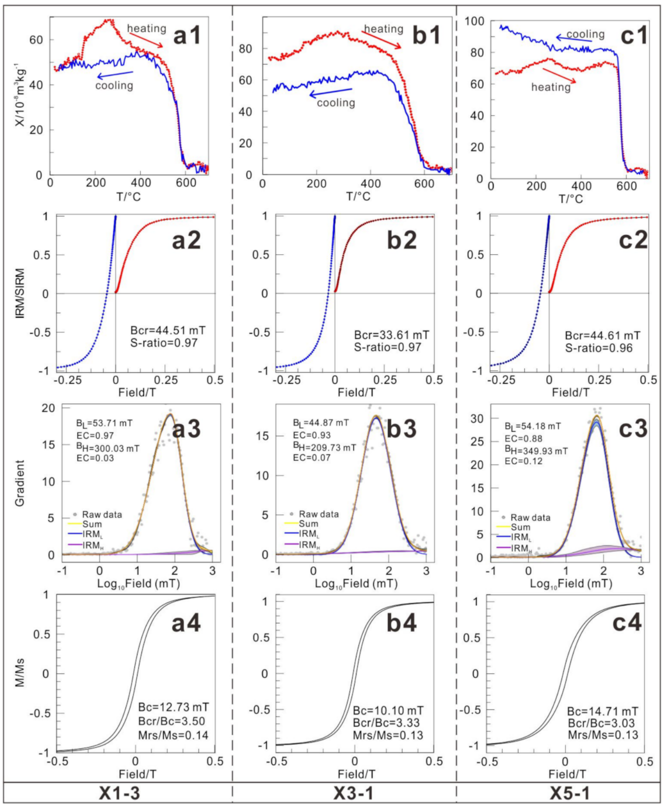

Figure 3. χ–T curves (**a1**–**c1**), isothermal remanent magnetization (IRM) acquisition and its back-field demagnetization curves (**a2**–**c2**), IRM component analysis (**a3**–**c3**), and hysteresis loops (**a4**–**c4**) for representative specimens. Bold (thin) lines represent heating (cooling) cycles (**a1**–**c1**). Green, purple, and yellow lines in (**a3**–**c3**) indicate the low-coercivity component (IRM_L), high-coercivity component (IRM_H), and the sum of IRM components. B_L, B_H, and EC refer to coercivity of the low-coercivity component, high-coercivity component and extrapolated contribution in (**a3**–**c3**), respectively. The open points represent the raw IRM gradient data in (**a3**–**c3**). The IRM acquisition curves, hysteresis loops are obtained in the applied field up to 1 T, but are cut off at 0.5 T for clarity.

3.3. Demagnetization of the Natural Remanent Magnetization (NRM)

All paleomagnetic specimens were subjected to stepwise thermal demagnetization using a PGL-100 thermal demagnetizer (PGL-100) [48]. The thermal demagnetization temperatures include 80, 150, 200, 250, 300, 320, 350, 390, 430, 460, 490, 520, 540, 560, 575, 585, 610 °C. This method was capable of isolating the characteristic remanent magnetization (ChRM) after removal of viscous remanent magnetization (VRM). The remanence measurements were performed using a Model 755 cryogenic magnetometer. (2-G Enterprises, Mountain View, CA, USA). Both the PGL-100 thermal demagnetizer and 2G-755 cryogenic magnetometer were housed in a magnetically shielded space with ambient field < 300 nT.

The principal component analyses (PCA) [49] were performed using the PaleoMag software [50]. The ChRM directions were determined with linear least squares fitting through the origin by using at least five continuous steps of demagnetization and with a maximum angular deviation (MAD) smaller than ~10°.

All the paleomagnetic and rock magnetic measurements were performed in the Paleomagnetism and Geochronology Laboratory (PGL), Institute of Geology and Geophysics, Chinese Academy of Sciences, Beijing, China.

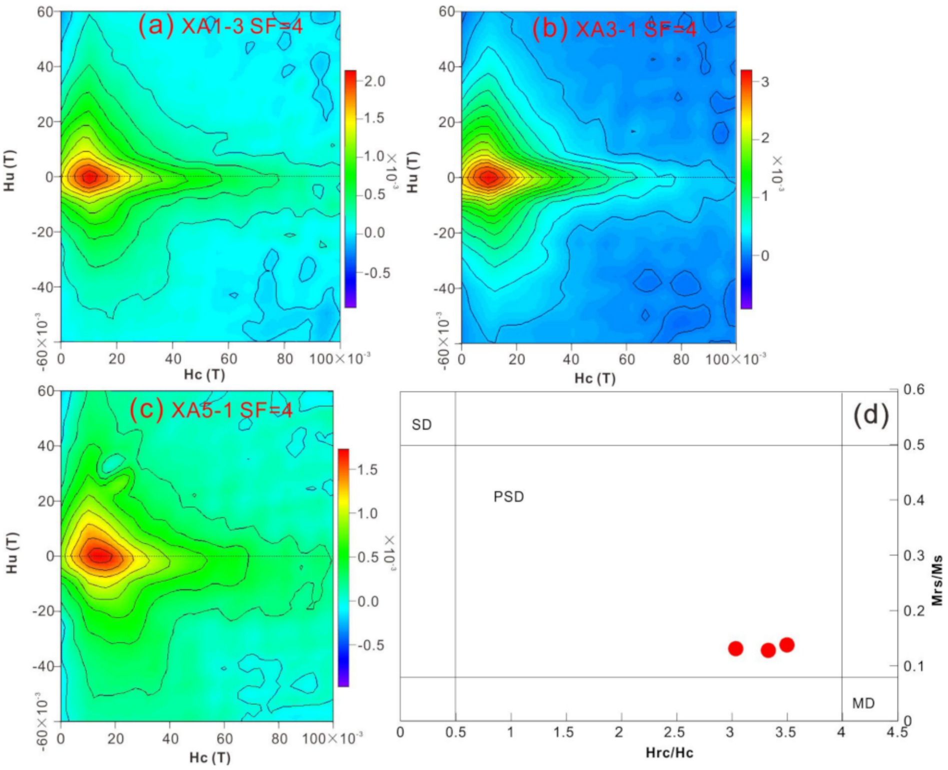

Figure 4. FORCs (**a**–**c**) and Day plot (**d**) of representative specimens from the Xing'antun section. SF, smoothing factor; SD, single domain; PSD, pseudo-single domain; MD, multidomain.

3.4. SIMS U–Pb Zircon Geochronology Analytical Method

Thin section studies show that tuff sample is weathered, in which feldspars are altered to clay minerals (Figure S1) and are not suitable for $^{40}Ar/^{39}Ar$ dating. Thus we separated zircons for SIMS U–Pb dating. Zircon grains from the tuff sample was processed by conventional magnetic and density techniques. Zircon grains, together with zircon standard Plesovice and Qinghu were mounted in epoxy mounts which were then polished to section the nearly half of the crystals. Cathodoluminescence (CL) images (Figure 6a) transmitted and reflected light micrographs were obtained prior to SIMS analyses, were conducted at the Institute of Geology and Geophysics, Chinese Academy of Sciences, Beijing.

Analyses were conducted using the Cameca IMS-1280 HR SIMS at Guangzhou Institute of Geochemistry, Chinese Academy of Sciences. U–Th–Pb ratios and absolute abundances were determined relative to the standard zircon Plesovice [51], analyses of which were interspersed with those of unknown grains, procedures similar to those described by [52]. Zircon standard Qinghu [53] measured as unknown to monitor the measurement procedures and data quality. A long-term uncertainty of 1.5% (1 RSD) for $^{206}Pb/^{238}U$ measurements of the standard zircons was propagated to the unknowns [54]. Corrections are sufficiently small to be insensitive to the choice of common Pb composition, and an average of present-day crustal composition [55] is used for the common Pb assuming that the common Pb is largely surface contaminated during sample preparation. Individual analyses' uncertainties in data tables are reported at a 1σ level. The SIMS U–Pb analytical results are listed in Table 2 and are further plotted as a U–Pb concordia diagram using the Isoplot/Ex v. 3.75 program [56] in Figure 6b.

Table 2. SIMS U–Pb zircon analysis.

					Conventional Concordia Columns (Pbc corr.)								
Sample/ Spot	**U (ppm)**	**Th (ppm)**	**Th/U (meas)**	**f_{206}%**	**$^{207}Pb/^{235}U$**	**±σ (%)**	**$^{206}Pb/^{238}U$**	**±σ (%)**	**ρ**	**$^{207}Pb/^{235}U$**	**±σ**	**$^{206}Pb/^{238}U$**	**±σ**
XAT15M2@01	658	299	0.455	0.44	0.111	2.56	0.0162	1.92	0.75	107.1	2.6	103.9	2.0
XAT15M2@02	494	202	0.409	0.21	0.110	2.55	0.0164	1.61	0.63	105.8	2.6	105.1	1.7
XAT15M2@04	751	266	0.354	0.76	0.108	4.07	0.0165	3.30	0.81	103.8	4.0	105.4	3.4
XAT15M2@05	1078	680	0.631	0.46	0.109	3.14	0.0164	1.67	0.53	104.9	3.1	105.0	1.7
XAT15M2@06	479	100	0.208	0.25	0.110	2.40	0.0169	1.88	0.78	106.0	2.4	107.7	2.0
XAT15M2@07	469	96	0.204	0.46	0.110	4.23	0.0165	3.85	0.91	106.3	4.3	105.3	4.0
XAT15M2@08	835	360	0.432	0.45	0.111	3.59	0.0163	2.46	0.68	107.3	3.7	104.0	2.5
XAT15M2@10	412	240	0.584	0.68	0.108	3.57	0.0164	1.75	0.49	103.8	3.5	105.1	1.8
XAT15M2@11	480	154	0.320	0.56	0.108	3.08	0.0168	1.75	0.57	103.8	3.0	107.4	1.9
XAT15M2@12	609	222	0.364	0.09	0.109	2.50	0.0158	2.07	0.83	105.1	2.5	101.3	2.1
XAT15M2@13	890	311	0.350	0.15	0.111	2.10	0.0165	1.68	0.80	106.7	2.1	105.4	1.8
XAT15M2@14	139	73	0.525	0.42	0.107	2.30	0.0166	1.66	0.72	103.5	2.3	106.2	1.8
XAT15M2@15	621	356	0.574	0.37	0.104	2.88	0.0163	2.41	0.84	100.7	2.8	104.3	2.5
XAT15M2@16	1679	794	0.473	0.16	0.110	3.71	0.0163	3.46	0.93	106.4	3.8	104.4	3.6
XAT15M2@17	525	480	0.915	0.18	0.112	2.04	0.0168	1.89	0.93	107.8	2.1	107.7	2.0
XAT15M2@18	400	152	0.381	0.21	0.109	3.20	0.0163	2.47	0.77	105.2	3.2	104.4	2.6
XAT15M2@19	473	211	0.446	0.12	0.112	1.96	0.0169	1.57	0.80	107.9	2.0	108.2	1.7
XAT15M2@20	892	244	0.274	0.38	0.108	2.34	0.0164	1.57	0.67	103.9	2.3	105.1	1.6
XAT15M2@21	702	52	0.074	0.45	0.112	3.42	0.0167	2.53	0.74	107.5	3.5	106.8	2.7
XAT15M2@22	345	107	0.310	0.55	0.112	3.95	0.0172	3.41	0.86	108.0	4.1	110.0	3.7
XAT15M2@23	1517	801	0.528	1.00	0.107	3.05	0.0166	1.62	0.53	103.0	3.0	105.9	1.7
XAT15M2@24	467	172	0.369	0.17	0.112	2.37	0.0165	2.10	0.89	108.0	2.4	105.8	2.2
XAT15M2@25	544	172	0.316	0.19	0.112	2.08	0.0170	1.86	0.89	107.4	2.1	108.9	2.0
XAT15M2@26	466	294	0.630	0.23	0.108	2.52	0.0161	1.95	0.77	104.4	2.5	103.0	2.0
XAT15M2@28	503	246	0.489	0.81	0.110	2.65	0.0170	2.11	0.80	106.0	2.7	108.9	2.3
XAT15M2@30	723	371	0.513	0.23	0.110	2.18	0.0168	1.63	0.75	106.0	2.2	107.1	1.7
XAT15M2@31	694	225	0.324	0.18	0.112	2.45	0.0165	1.71	0.70	107.5	2.5	105.3	1.8
XAT15M2@32	1071	585	0.547	7.51	0.105	8.26	0.0162	1.85	0.22	101.7	8.0	103.7	1.9
XAT15M2@03	367	204	0.557	1.34	0.100	4.60	0.0159	1.73	0.38	96.5	4.2	101.6	1.7
XAT15M2@09	361	144	0.400	0.31	0.126	4.51	0.0184	4.10	0.91	120.9	5.2	117.8	4.8
XAT15M2@29	1098	469	0.428	0.12	0.199	5.13	0.0274	4.50	0.88	184.3	8.7	174.5	7.8

4. Results

4.1. Rock Magnetism

All the χ–T curves display a clear and major susceptibility drop near 585 °C (Figure 3), the Curie point of magnetite, suggesting that magnetite is the major contributor to the susceptibility. The value of χ is almost the same (Figure 3) or changes slightly (<20 $\times$ 10^{-8} m^3kg^{-1}) (Figure 3(b1,c1)) after heating and cooling, indicating that no significant changes in magnetic mineralogy have occurred during thermal treatment [57].

The heating curve displays a slight hump at around 300 °C (Figure 3). The susceptibility increases from 200 °C to 300 °C might be due to the production of maghemite (γFe_2O_3) from some less magnetic Fe-hydroxides during heating (e.g., lepidocrocite, γFeOOH) [57,58]. Subsequently, the susceptibility decreases from 300 °C to 400 °C can be interpreted as the conversion of newly produced maghemite to the weakly magnetic hematite (αFe_2O_3) [57].

The IRM acquisition curves (Figure 3(a2–c2)) show that remanence of more than 80% was obtained at 200 mT and all of them were already close to saturation at 300 mT. The S-ratio is close to one (generally above 0.96). The hysteresis loops (Figure 3(a4–c4)) are closed above ~300 mT, indicating the dominance of low-coercivity ferrimagnetic minerals. IRM component analyses (Figure 3(a3–c3)) further confirm the results. The low-coercivity component of IRM (IRM_L) accounts for the main contribution, while the high-coercivity component of IRM (IRM_H) can be ignored. Combined with the behaviors of the χ–T curves, it can be seen that the low-coercivity component is magnetite.

The contours on the FORCs diagram (Figure 4a–c) have a remarkable vertical spread, showing a clear manifestation of magnetostatic interactions. The inner contours display a distinct, closed-contour peak structure on the Hu = 0 axis between 10 and 15 mT, with some vertical spread in the FORC distribution. Meanwhile, the outer contours diverge from the Hu = 0 axis and intersect with the Hc = 0 axis, displaying less symmetry and a divergent pattern, which extends less than 60 mT. Therefore, these FORC diagrams have distinct closed contours, but the contours are divergent and less symmetrical, lie closer to the origin trend, and are spread out along the Hu axis, both displaying interacting SD-like behavior and showing MD-like FORC distributions, demonstrating characteristic coarse PSD magnetite grains behavior [59,60]. The Day plot (Figure 4d) further supports the results; it was plotted in the PSD area but close to the MD area.

4.2. Paleomagnetic Results

Representative demagnetization diagrams are shown by orthogonal diagrams [61] and associated remanence decay curves in Figure 5. For all specimens of the Xing'antun section, a secondary magnetic component, probably of viscous origin, was removed by thermal demagnetization at ~300 °C (the black and blue dots). The high-stability ChRM component can be separated between 300 °C and 585 °C (the red dots). The mean direction of the ChRM after tilt correction is Ds = 46.5° (± 18.1°), Is = 59.3° (± 9.3°), n = 24, k = 11.2, α95 = 9.3°, which stay away from present geomagnetic position (D = −10.83°, I = 61.12°) in the equal-area projections (Figure S2), suggesting that the CHRM is primary remanent magnetization. At least four contiguous specimens with a stable characteristic remanence direction are necessary to identify a magnetic polarity interval. Following stepwise demagnetization, the studied specimens are of normal polarity except for one specimen with negative inclination; thus only one normal magnetozone (N1) was recognized in the Xing'antun section.

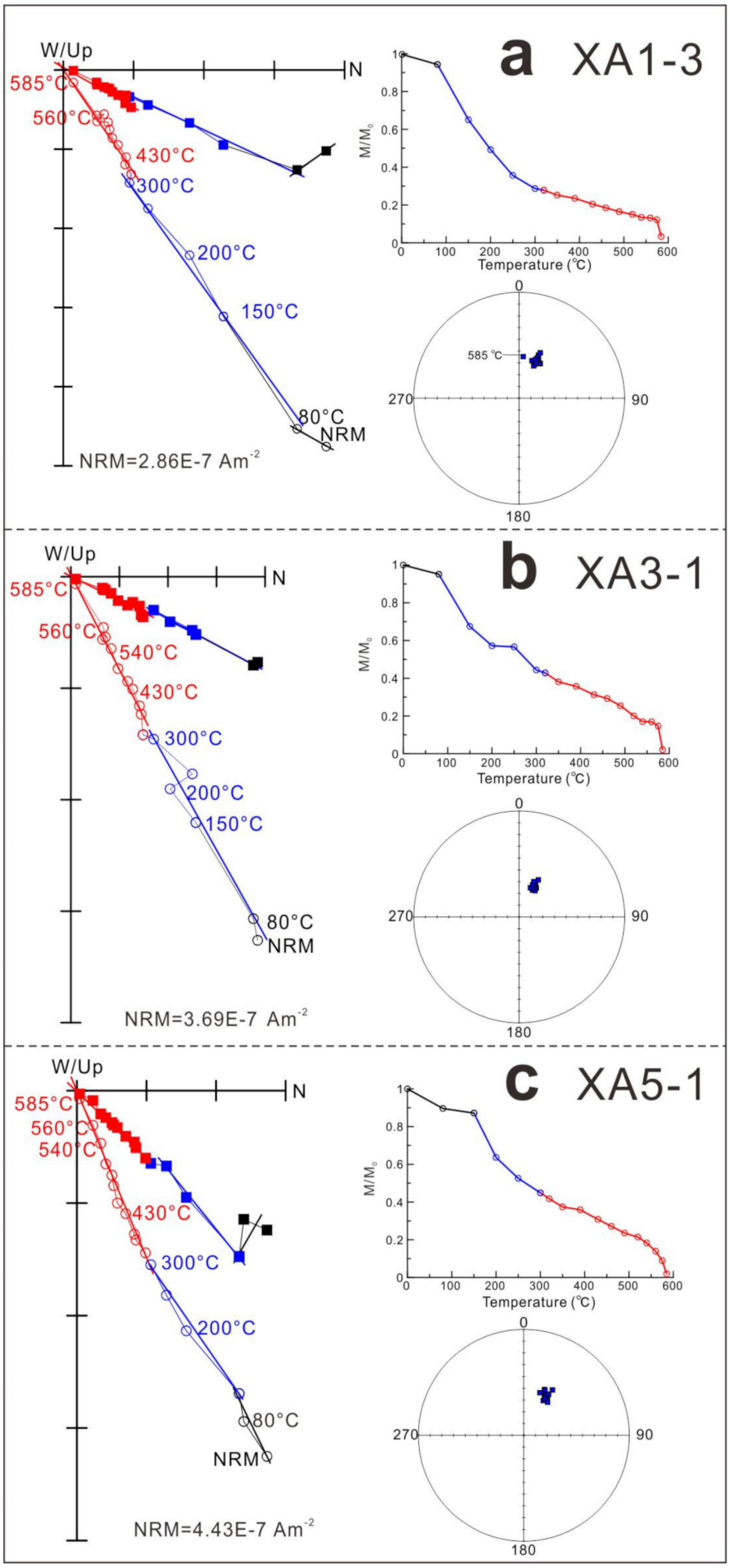

Figure 5. The direction and intensity evolution of the NRM during stepwise thermal demagnetization for representative specimens of the Xing'antun section. Open and Solid symbols in the orthogonal vector endpoint projections [61] indicate projections on the vertical and horizontal planes in stratigraphic coordinates, respectively. The red/blue points show the thermal temperature intervals used for isolating the ChRM/VRM. NRM is the natural remanent magnetization.

4.3. SIMS U–Pb Zircon Geochronology

Sample XAT15M2 yields euhedral to subhedral zircons with a range of sizes from 80 to 190 μm in length. Zircon grains from this sample are relatively transparent and colorless. All of the analyses were conducted on portions of zircon with oscillatory zoning, which is interpreted as reflecting growth in magma. Thirty-two zircon grains were analyzed from this sample, U and Th contents are within the range 139–1679 ppm and 52–801 ppm, respectively, with Th/U ratios of 0.204–0.915. One analysis (spot 03, Table 2) has a relatively young age, interpreted as a result of Pb loss. Two spots (spots 09 and 29) yield older than the ages of most zircon grains of this sample interpreted as xenocrysts from the Quanshuicun Formation [33]. The remaining twenty-eight analyses obtained a concordia U–Pb age of 105.7 ± 0.8 Ma and the $^{206}Pb/^{238}U$ weighted mean age of 105.7 ± 0.8 Ma (MSWD = 0.8, 2σ internal error reported here and after unless otherwise noted) (Figure 6a), which is interpreted as the crystallization age of zircons from the sample XAT15M2.

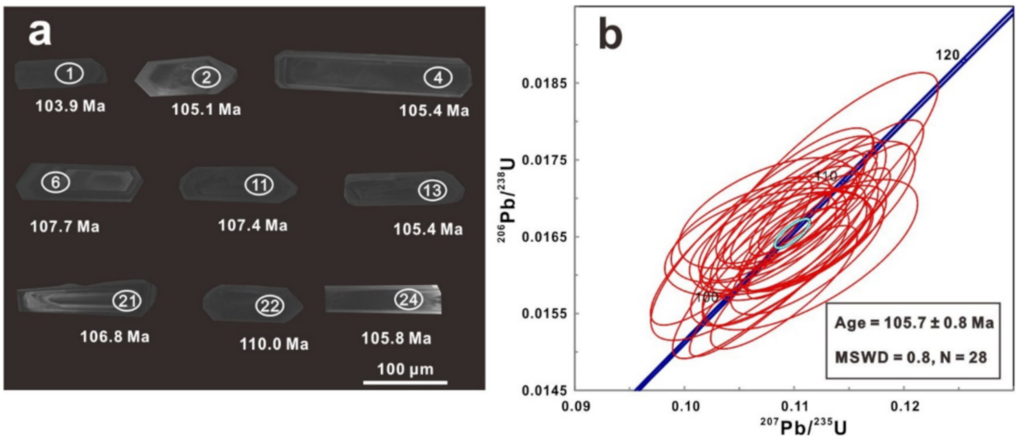

Figure 6. Representative CL images (**a**) and SIMS U–Pb concordia age plot (**b**) for zircons from the Xing'antun section. Data-point error ellipses are 2σ level.

5. Discussion

5.1. New Geochronologic Constraints on the Dalazi Formation in the Yanji Basin

Previous geochronologic constraints on the Dalazi Formation in the Yanji Basin were mainly based on lithostratigraphy and biostratigraphy [21,25,39] or indirectly constrained by the radiometric dating results from the overlying Longjing Formation and the underlying Quanshuicun Formation. However, direct age constraints on the Dalazi Formation remain poorly known [26,39]. The lack of precise age constraints of the Dalazi Formation limits our understanding of Early Cretaceous terrestrial processes and the regional stratigraphic correlations.

The Dalazi Formation has been suggested to be formed during the early Early Cretaceous [62], middle and late Early Cretaceous [21], or late Early Cretaceous [26,36], and even extending to early Late Cretaceous [25,34], based on lithostratigraphic and biostratigraphic studies. For example, a detailed taxonomic study of ostracod species from the Dalazi Formation of the Yanji Basin was conducted by Choi et al. [25], who suggest that the age of this formation is not older than the Albian age, probably of early Late Cretaceous age. Sun et al. [32,33] reported a series of LA-ICP-MS (laser ablation ion coupled plasma mass spectrometry) U–Pb zircon dates from the Tuntianying and Quanshuicun formations, and they proposed that the age of the base of the Quanshuicun Formation is 116.8 ± 1.4 Ma, providing a maximum age estimates of the base of the Dalazi Formation in the Yanji Basin. These results showed a large discrepancy in the age of the Dalazi Formation. Direct radiometric dating of the Dalazi Formation will help to address this problem.

Recently, the bottom and top of the Dalazi Formation in Jilin Province were estimated at 109.9 ± 2.9 to 93.5 ± 1.2 Ma based on the LA-ICP-MS U–Pb dating of tuffs [63]. These ages provide a preliminary duration of the Dalazi Formation. However, a tuff sample collected from the overlying Longjing Formation was successfully dated by a CA–ID–TIMS (chemical abrasion–isotope dilution–thermal ion mass spectrometry) U–Pb zircon method in UC-Davis, yielding an age of 101.039 ± 0.061 Ma [35]. Most recently, Zhong et al. [26] reported three SIMS U–Pb zircon ages from tuff beds of the uppermost part of the Dalazi Formation in the Yanji Basin, yielding a weighted mean $^{206}Pb/^{238}U$ ages of 105.1 ± 0.4 Ma.

In this study, one tuff bed collected from the Xing'antun section of the upper part of the Dalazi Formation yielded a weighted mean $^{206}Pb/^{238}U$ age of 105.7 ± 0.8 Ma, which could be interpreted as the deposition age of the sediments (Figures 6 and 7). The U–Pb age lies precisely in the Cretaceous Normal Superchron (CNS, chron C34n) period, thus providing tight age controls on the Xing'antun section. Considering these geochronologic constraints, the recognized normal magnetozone N1 can be correlated to early C34n between chron M"-2r" (~107.5 Ma) and chron M"-3r" (~103 Ma) [42] (Figure 7). Thus, the age of the sedimentary sequence of the Xing'antun section can be precisely constrained to be 107.5–103 Ma.

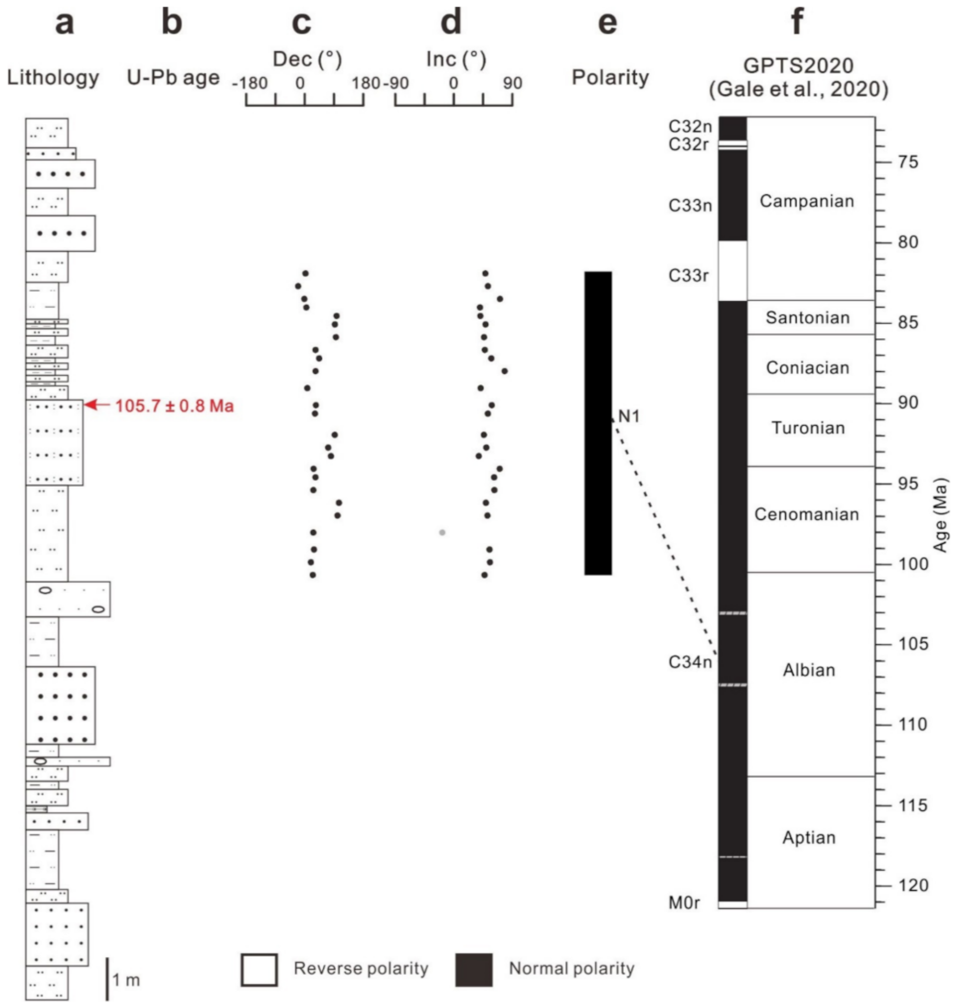

Figure 7. Lithostratigraphy, magnetostratigraphy, and SIMS U–Pb zircon chronology of the Xing'antun section in the Yanji Basin. (**a**–**f**): Lithology, U–Pb age, declination (Dec.), inclination (Inc.), polarity zonation of the Xing'antun section, and reference geomagnetic polarity timescale (GPTS) (Gale et al., 2020, [42]).

The new age acquired from our new SIMS U–Pb zircon dating is consistent with that of Zhong et al. [26] in consideration of the uncertainty of the dating method (~1%, [34]). Furthermore, our new magnetostratigraphic study of the Xing'antun section provides a more comprehensive understanding of geochronologic framework of the Dalazi Formation. The established geochronologic framework of the Dalazi Formation enables precise correlation of the terrestrial Lower Cretaceous in the Yanji Basin to global marine strata and other continental sequences (Figure 8).

5.2. Stratigraphic Correlation to Other Continental Rift Basins in Northeastern China and its Tectonic Implication

During the late Mesozoic period, a number of continental rift basins were formed in northeastern China due to tectonic and magmatic activities, such as the Songliao, Dasanjiang, Hailaer and Jixi basins and they provide a rare opportunity to investigate the basin evolutionary history of the active plate regime (e.g., [6,64,65]. The Cretaceous sedimentary basins in NE China can be subdivided into two stages: syn-rift and post-rift stages (Figure 8). An understanding of the continental rift basins' stratigraphic development can help to reveal the tectonic processes in NE China during this time.

According to previous research [32,33], the age of the uppermost part of the Tuntianying Formation is 125 ± 2.7 Ma, and the age of the base of the Quanshuicun Formation is 116.8 ± 1.4 Ma. The upper part of the Dalazi Formation is precisely dated to 105.7 Ma in this study and in previous studies [26], and the lower part of the overlying Longjing Formation was precisely dated at 101.039 Ma (Figure 8b) [35]. The established geochronologic framework of the Cretaceous strata in the Yanji Basin enables regional correlation.

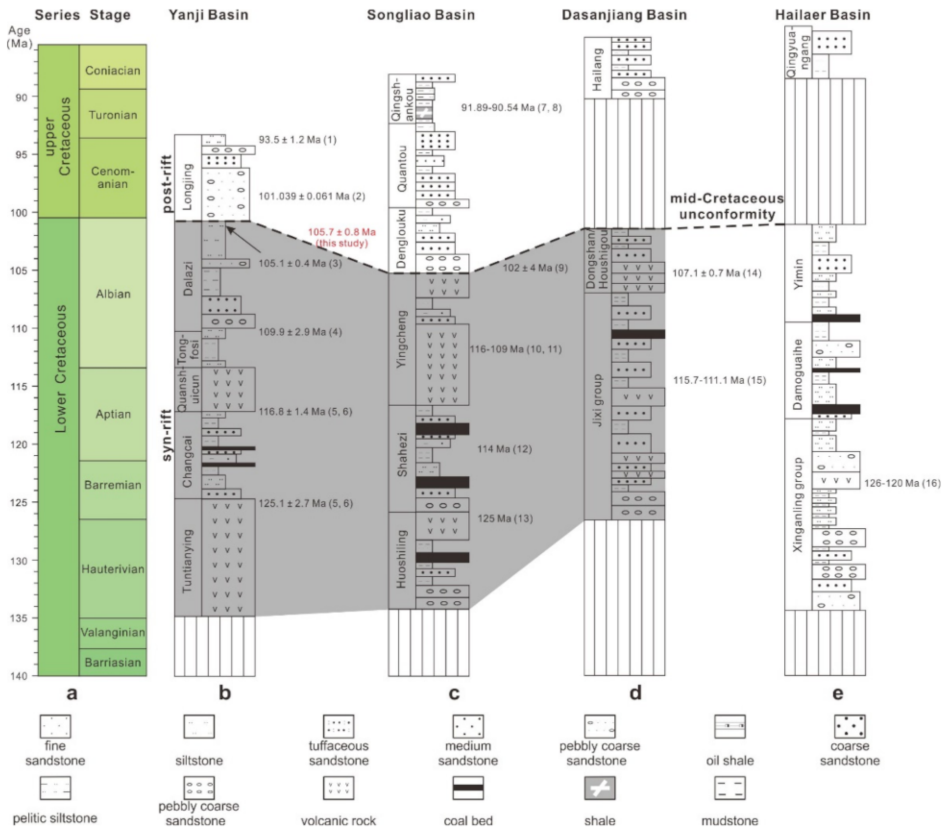

Figure 8. Regional correlation of the terrestrial Cretaceous strata in the Yanji Basin to the those from other representative basins in northeastern China. Geologic timescale 2020 [42] (**a**); chronostratigraphy of the Yanji (**b**), Songliao (**c**), Dasanjiang (**d**), and Hailaer (**e**) basins. References: (1): [34]; (2): [11]; (3): [26]; (4): [34]; (5): [32]; (6): [33]; (7): [3]; (8): [66]; (9): [67]; (10): [68]; (11): [69]; (12): [8]; (13): [70]; (14): [71]; (15): [72]; (16): [73].

Previous studies show a major unconformity between the syn-rift and post-rift stages in adjacent areas of the Yanji Basin, such as the Songliao, Dasanjiang, and Hailaer basins in northeastern China. Research on the Cretaceous Continental Scientific Drilling (CCSD-

SK) borehole in the Songliao Basin has advanced our knowledge of major stratigraphic boundaries and facilitated regional stratigraphic correlation. The youngest age obtained by detrital zircon LA-ICP-MS U–Pb dating was that of the second member of the Denglouku Formation from the CCSD-SK-IIe borehole in the Songliao Basin, which is 102 ± 4 Ma [67]. Thus, the upper part of the Dalazi Formation in the Yanji Basin is clearly correlated with the lower Denglouku Formation in the Songliao Basin (Figure 8b,c). Moreover, the ostracod results suggest that both the Dalazi Formation in the Yanji Basin and the Denglouku Formation in the Songliao Basin record a *Cypridea* (*Morinina*)–*Bisulcocypridea–Mongolocypris* assemblage [74], which also supports the above correlation.

This correlation was strengthened by the overlying and underlying lithological formations in the two basins. The Quanshuicun Formation in the Yanji Basin is correlated to the Yingcheng Formation in the Songliao Basin based on the geochronologic evidence [6,68–70]. Combined with biostratigraphic and zircon U–Pb dating results, the Longjing Formation in the Yanji Basin is correlated with the Quantou Formation in the Songliao Basin [11,43].

There existed a unified basin in the Dasanjiang area in northeastern China during the Early Cretaceous, based on the geologic evidence and drilling core observations (e.g., [69]), which consists of the Sanjiang, Boli, Jixi and Hegang basins. Recently, Zhang et al. [71] proposed that the age of the Dongshan Formation is 107.1 ± 0.7 Ma based on LA-ICP-MS U–Pb zircon dating of an andesite sample from the ZK2 borehole in the eastern Boli Basin (Figure 8d). Despite the uncertainty of the LA-ICP-MS and SIMS U–Pb zircon dating methods [63], the Dongshan Formation is clearly correlated to the Dalazi Formation and the paleontological analysis also supports this correlation [75] (Figure 8b,d). Zircons from two tephra samples of the Chengzihe Formation from the Jixi Basin were analyzed by the LA-ICP-MS dating method, yielding ages between 115.7 ± 1.0 and 111.1 ± 1.1 Ma [72]. This age range suggests that the Quanshuicun Formation is correlated to the Chengzihe Formation in the Sanjiang Basin.

Apart from the Yanji Basin, the Lower Cretaceous in the Hailaer Basin is well developed. Paleontological data (e.g., ostracods, phytoplanktons, sporopollens) indicate the latest Early Cretaceous age for the Yimin Formation in the Hailaer Basin, which is a similar geologic period as the Dalazi Formation in the Yanji Basin [76]. No precise radioisotopic ages are, however, available for the Yimin Formation in the Hailaer Basin. Underlying the Yimin Formation, a set of LA-ICP-MS U–Pb zircon ages of 126 ± 1 Ma to 120 ± 1 Ma have been obtained in volcanic rocks from the Lower Cretaceous Xing'anling Group in the Hailaer Basin [73], which is similar to the age of the Huoshiling Formation in the Songliao Basin, and the Tuntianying Formation in the Yanji Basin.

Our results indicate that the upper part of the Dalazi Formation in the Yanji Basin in northeastern China is of late Albian age. This unit is precisely correlated with the Denglouku Formation in the Songliao Basin, and it is approximately correlated with the middle-upper part of the Dongshan Formation in the Dasanjiang Basin, and with the Yimin Formation in the Hailaer Basin in northeastern China (Figure 8).

Provenance changes across the mid-Cretaceous unconformity between the syn-rift and post-rift stages in northeastern China have been observed [13,31,77]. For example, the underlying Yincheng Formation and the overlying Denglouku Formation in the Songliao Basin (Figure 8c); the underlying Dongshan/Houshigou Formation and the overlying Hailang Formation in the Dasanjiang Basin (Figure 8d); and the underlying Yimin Formation and the overlying Qingyuangang Formation in the Hailaer Basin (Figure 8e). However, the precise age of this tectonic activity in these basins was poorly constrained by detrital zircon geochronology (e.g., [67,77]), and biostratigraphy (e.g., [25]), and indirectly constrained by geochronologic studies of underlying and overlying volcanic rocks (e.g., [32,33]).

The stratigraphic record, previous studies on regional unconformity between the Dalazi and Longjing formations, and our new chronology of the Dalazi Formation show that mid-Cretaceous unconformity is recorded in the mid-Cretaceous Yanji Basin, which is consistent with the tectono-sedimentary evolution of adjacent volcanic-sedimentary basins. The age of this tectonic activity in the Yanji Basin is precisely constrained to ~106–101

Ma [35]. A tectonic switch from extension to contraction might result from the process of the subduction of the Paleo–Pacific plate beneath the Eurasia plate, that is, from slab rollback to NW–SE direction subduction during this time [13,65,77]. Further provenance studies between the Dalazi and Longjing formations in the Yanji Basin and precise radiometric dates from neighboring continental rift basins, such as the Songliao, Dasanjiang, and Hailaer basins, will broaden our knowledge of this tectonic activity and its implications for the nature of the continental margin evolution of northeast Asia during the late Mesozoic.

6. Conclusions

We carried out magnetostratigraphic and geochronologic investigations on a volcanic–sedimentary sequence and a tuff sample from the Xing'antun section of the Yanji Basin, northeastern China. Systematic rock magnetic measurements and stepwise thermal demagnetization indicate that the main carrier for the ChRM is mainly PSD magnetite. Zircons from the tuff sample were analyzed by the SIMS U–Pb zircon dating method, yielding a weighted mean $^{206}Pb/^{238}U$ age of 105.7 ± 0.8 Ma (2σ, internal error). One recognized magnetozone of normal polarity in this outcrop section is correlated with chron C34n constrained by the U–Pb age. This new, integrated chronostratigraphy suggests that the upper part of the Dalazi Formation in the Yanji Basin is precisely dated at 105.7 Ma, corresponding to the late Albian age, which enables precise correlation of the terrestrial Upper Cretaceous of the Yanji Basin to other continental sequences in northeastern China.

The establishment of the chronologic framework for the upper part of the Dalazi Formation in the Yanji Basin allows regional correlation with the terrestrial strata from other rift basins in northeastern China. Combining our new chronology and previous provenance and geochronologic studies with the regional correlation of adjacent sedimentary basins, we suggest that the mid-Cretaceous unconformity was recorded between the Dalazi and Longjing formations in the Yanji Basin, and its age can be constrained to ~106–101 Ma.

Supplementary Materials: The following are available online at https://www.mdpi.com/article/10.3390/min11050527/s1, Figure S1: Photomicrographs of XAT15M2 viewed under planepolarized light and cross-polarized light, Figure S2: Equal-area projections of the sample-mean direction for ChRM after tilt correction.

Author Contributions: Z.S. and Z.Y. designed research; Z.S., Z.Y., H.Y., Z.Q., and D.X., performed research; Z.S., Z.Y., and H.Y., analyzed data; and Z.S., Z.Y., H.Y., Z.Q., and D.X., wrote the paper. All authors have read and agreed to the published version of the manuscript.

Funding: This research was funded by the National Natural Science Foundation of China (grants 41688103, 41888101, and 41790452), Key Research Program of Frontier Sciences, CAS (ZDBS-LY-DQC002), the Strategic Priority Program (A) of the Chinese Academy of Sciences (Grant No. XDA17010204), and the Strategic Priority Program (B) of the Chinese Academy of Sciences (Grant No. XDB18030505).

Data Availability Statement: Not applicable.

Acknowledgments: We thank the Editors and three anonymous reviewers for their insightful comments and suggestions, to improve the manuscript. We are grateful to Mengjie Wang for field assistance. We thank Qiuli Li, Xiaoping Xia, Huafeng Qin, Shuangchi Liu, Qing Yang, Zexian Cui for their support and advice during the SIMS zircon U–Pb analysis and paleomagnetic analysis.

Conflicts of Interest: The authors declare no conflict of interest.

References

1. Zhou, Z.H.; Barrett, P.M.; Hilton, J. An exceptionally preserved Lower Cretaceous ecosystem. *Nature* **2003**, *421*, 807–814. [CrossRef] [PubMed]
2. Yang, S.H.; He, H.Y.; Jin, F.; Zhang, F.C.; Wu, Y.B.; Yu, Z.Q.; Li, Q.L.; Wang, M.; O'Connor, J.K.; Deng, C.L.; et al. The appearance and duration of the Jehol Biota: Constraint from SIMS U-Pb zircon dating for the Huajiying Formation in northern China. *Proc. Natl. Acad. Sci. USA* **2020**, *117*, 14299–14305. [CrossRef] [PubMed]
3. He, H.Y.; Deng, C.L.; Wang, P.J.; Pan, Y.X.; Zhu, R.X. Toward age determination of the termination of the Cretaceous Normal Superchron. *Geochem. Geophys. Geosyst.* **2012**, *13*, 02002. [CrossRef]

4. Deng, C.L.; He, H.Y.; Pan, Y.X.; Zhu, R.X. Chronology of the terrestrial Upper Cretaceous in the Songliao Basin, northeast Asia. *Palaeogeogr. Palaeoclim. Palaeoecol.* **2013**, *385*, 44–54. [CrossRef]
5. Wang, C.S.; Scott, R.W.; Wan, X.Q.; Graham, S.A.; Huang, Y.J.; Wang, P.J.; Wu, H.C.; Dean, W.E.; Zhang, L.M. Late Cretaceous climate changes recorded in Eastern Asian lacustrine deposits and North American Epieric sea strata. *Earth-Sci. Rev.* **2013**, *126*, 275–299. [CrossRef]
6. Xi, D.P.; Wan, X.Q.; Li, G.B.; Li, G. Cretaceous integrative stratigraphy and timescale of China. *Sci. China Earth Sci.* **2019**, *62*, 256–286. [CrossRef]
7. Yu, Z.Q.; He, H.Y.; Deng, C.L.; Xi, D.P.; Qin, Z.H.; Wan, X.Q.; Wang, C.S.; Zhu, R.X. New geochronological constraints for the Upper Cretaceous Nenjiang Formation in the Songliao Basin, NE China. *Cretac. Res.* **2019**, *102*, 160–169. [CrossRef]
8. Yu, Z.Q.; He, H.Y.; Deng, C.L.; Lu, K.; Shen, Z.S.; Li, Q.L. New SIMS U-Pb geochronology for the Shahezi Formation from CCSD-SK-IIe borehole in the Songliao Basin, NE China. *Sci. Bull.* **2020**, *65*, 1049–1051. [CrossRef]
9. Zhu, R.X.; Xu, Y.G.; Zhu, G.; Zhang, H.F.; Xia, Q.K.; Zheng, T.Y. Destruction of the North China Craton. *Sci. China Earth Sci.* **2012**, *55*, 1565–1587. [CrossRef]
10. Gao, Y.; Ibarra, D.E.; Wang, C.S.; Caves, J.K.; Chamberlain, C.P.; Graham, S.A.; Wu, H.C. Mid-latitude terrestrial climate of East Asia linked to global climate in the Late Cretaceous. *Geology* **2015**, *43*, 287–290. [CrossRef]
11. Zhang, L.M.; Wang, C.S.; Wignall, P.B.; Kluge, T.; Wan, X.Q.; Wang, Q.; Gao, Y. Deccan volcanism caused coupled pCO2 and terrestrial temperature rises, and pre-impact extinctions in northern China. *Geology* **2018**, *46*, 271–274. [CrossRef]
12. Wan, X.Q.; Zhao, J.; Scott, R.W.; Wang, P.J.; Feng, Z.H.; Huang, Q.H.; Xi, D.P. Late Cretaceous stratigraphy, Songliao Basin, NE China: SK1 cores. *Palaeogeogr. Palaeoclim. Palaeoecol.* **2013**, *385*, 31–43. [CrossRef]
13. Li, S.Q.; He, S.; Chen, F.K. Provenance changes across the mid-Cretaceous unconformity in basins of northeastern China: Evidence for an integrated paleolake system and tectonic transformation. *Geol. Soc. Am. Bull.* **2020**, *133*, 185–198. [CrossRef]
14. Li, Y.J.; He, H.Y.; Deng, C.L.; Pan, Y.X.; Ji, Q.; Wang, C.S.; Zheng, D.W.; Zhu, R.X. $^{40}Ar/^{39}Ar$ dating results from the Shijiatun Formation, Jiaolai Basin: New age constraints on the Cretaceous terrestrial volcanic-sedimentary sequence of China. *Cretac. Res.* **2018**, *86*, 251–260. [CrossRef]
15. Han, F.; Sun, J.P.; Qin, H.F.; Wang, H.P.; Ji, Q.; He, H.Y.; Deng, C.L.; Pan, Y.X. Magnetostratigraphy of the Upper Cretaceous and Lower Paleocene terrestrial sequence, Jiaolai Basin, eastern China. *Palaeogeogr. Palaeoclim. Palaeoecol.* **2020**, *538*, 109451. [CrossRef]
16. Wilf, P.; Johnson, K.R.; Huber, B.T. Correlated terrestrial and marine evidence for global climate changes before mass extinction at the Cretaceous-Paleogene boundary. *Proc. Natl. Acad. Sci. USA* **2003**, *100*, 599–604. [CrossRef] [PubMed]
17. Scotese, C.R.; Song, H.; Mills, B.J.; van der Meer, D.G. Phanerozoic paleotemperatures: The earth's changing climate during the last 540 million years. *Earth-Sci. Rev.* **2021**, *215*, 103503. [CrossRef]
18. Haq, B.U.; Hardenbol, J.; Vail, P.R. Chronology of Fluctuating Sea Levels since the Triassic. *Science* **1987**, *235*, 1156–1167. [CrossRef] [PubMed]
19. Haq, B.U. Cretaceous eustasy revisited. *Glob. Planet. Chang.* **2014**, *113*, 44–58. [CrossRef]
20. Chang, M.M.; Chou, C.C.; Liu, C.C. The age and depositional environment of Cretaceous fish–bearing strata of Northeast China. *Vertebr. Palasiat.* **1977**, *15*, 194–197, (In Chinese with English Abstract).
21. Zhou, Z.Y.; Chen, P.J.; Li, B.X.; Li, W.B.; Wen, S.X.; Zhang, L.J.; Ye, M.N.; Liu, Z.S.; Li, Z.P.; Yang, X.L. Younger Mesozoic non-marine deposits of the Yanbian area, eastern Jilin. *Bull. Nanjing Inst. Geol. Palaeontol. Acad. Sin.* **1980**, *1*, 1–21.
22. Li, G.Q. Discovery of the Chinese Bowfin in Eastern Jilin. *Acta Vertebr. Sin.* **1984**, *22*, 67–94, (In Chinese with English Abstract).
23. Li, G.Q. A new genus of Hiodontidae from Luozigou basin, Easte Jilin. *Vertebr. Palasiat.* **1987**, *25*, 91–107, (In Chinese with English Abstract).
24. Tao, J.R.; Zhang, C.B. Early Cretaceous angiosperms of the Yanji basin, Jilin province. *Acta Bot. Sin.* **1990**, *32*, 220–229.
25. Choi, B.D.; Wang, Y.Q.; Hu, L.; Huh, M. Ostracod faunas from the Dalazi and Tongfosi formations (Yanji Basin, northeast China): Biostratigraphic, palaeogeographic and palaeoecological implications. *Cretac. Res.* **2020**, *105*, 104018. [CrossRef]
26. Zhong, Y.T.; Wang, Y.Q.; Jia, B.Y.; Wang, M.; Hu, L.; Pan, Y.H. A potential terrestrial Albian–Cenomanian boundary in the Yanji Basin, Northeast China. *Palaeogeogr. Palaeoclim. Palaeoecol.* **2021**, *562*, 110088. [CrossRef]
27. Yang, X.J.; Deng, S.H. Discovery of Pseudofrenelopsis gansuensis from the Lower Cretaceous of Wangqing, Jilin Province, and its significance in correlation of Cretaceous red beds in China. *Acta Geol. Sin. Engl. Ed.* **2007**, *81*, 905–910.
28. Xu, Q.; Yang, X.J. Preliminary Study of Flora from the Upper Lower Cretaceous Dalazi Formation in Luozigou Basin, Wangqing, Jilin Province, Northeast China. *Open J. Geol.* **2019**, *9*, 581–584. [CrossRef]
29. Deng, S.H.; Lu, Y.Z.; Fan, R.; Li, X.; Liu, L. Cretaceous floras and biostratigraphy of China. *J. Stratigr.* **2012**, *36*, 241–265, (In Chinese with English Abstract).
30. Zhang, J.G.; Qiao, D.W.; Jin, Y.J.; Liu, Y.J.; Deng, C.W.; Cong, P.H.; Zhang, D.H. Multi-unconformity stage and its oil-gas geological significance in the Yanji Basin. *J. Jilin Univ. Earth Sci. Ed.* **2013**, *43*, 1772–1778, (In Chinese with English Abstract).
31. Zhu, J.C.; Meng, Q.R.; Feng, Y.L.; Yuan, H.Q.; Wu, F.C.; Wu, H.B.; Wu, G.L.; Zhu, R.X. Decoding stratigraphic evolution of the Hailar Basin: Implications for the late Mesozoic tectonics of NE China. *Geol. J.* **2020**, *55*, 1750–1762. [CrossRef]
32. Sun, Y.W.; Liu, H.; Wan, C.B.; Quan, C. In situ spores of Asplenium and their implications for the evolution of the Aspleniaceae: A case study from the Lower Cretaceous Changcai Formation in eastern Jilin Province, China. *Cretac. Res.* **2010**, *31*, 424–432. [CrossRef]

33. Sun, Y.W.; Li, X.; Zhao, G.W.; Liu, H.; Zhang, Y.L. Aptian and Albian atmospheric CO_2 changes during oceanic anoxic events: Evidence from fossil Ginkgo cuticles in Jilin Province, Northeast China. *Cretac. Res.* **2016**, *62*, 130–141. [CrossRef]
34. Li, X.; Gao, Y.; Zhang, D.J.; Ding, H.S.; Yang, Z.Y.; Sun, Y.W. U-Pb age of the Dalazi Formation in the Zhixin Basin, Yanbian, Jilin. In Proceedings of the 28th Annual Academic Conference of the PSC, Shenyang, China, 11–14 August 2015; pp. 165–166.
35. Zhang, L.Z.; Jin, C.Z.; Yin, Q.Z.; Huyskens, M.; Jin, D.C.; Zhang, J.L.; Jin, F.; Xu, X. A new dinosaur fossil locality of Mid-Cretaceous age in northeastern China. In Proceedings of the Society of Vertebrate Palaeontology 78th Annual Meeting, Albuquerque, NM, USA, 17–20 October 2018; p. 236.
36. Zhang, G.F. Discussion on the geological age of the Dalazi Formation in Jilin province, China. *J. Stratigr.* **2005**, *29*, 381–388.
37. Li, X.M.; Gong, G.L. Constraints from fission track thermochronology for geological age of Dalazi Formation in Jilin Province, China. *At. Energy Sci. Technol.* **2008**, *42*, 565–567.
38. Wu, F.Y.; Sun, D.Y.; Ge, W.C.; Zhang, Y.B.; Grant, M.L.; Wilde, S.A.; Jahn, B.M. Geochronology of the Phanerozoic granitoids in northeastern China. *J. Asian Earth Sci.* **2011**, *41*, 1–30. [CrossRef]
39. Li, G.; Ohta, T.; Batten, D.J.; Sakai, T.; Kozai, T. Morphology and phylogenetic origin of the spinicaudatan Neodiestheria from the Lower Cretaceous Dalazi Formation, Yanji Basin, north-eastern China. *Cretac. Res.* **2016**, *62*, 183–193. [CrossRef]
40. Teng, X.; Li, G. Clam shrimp genus Ordosestheria from the Lower Cretaceous Dalazi Formation in Jilin Province, north-eastern China. *Cretac. Res.* **2017**, *78*, 196–205. [CrossRef]
41. Sun, G.; Zheng, S.L. New proposal on division and correlation of Mesozoic from northeastern China. *J. Stratigr.* **2000**, *24*, 60–64, (In Chinese with English Abstract).
42. Gale, A.S.; Mutterlose, J.; Batenburg, S.; Gradstein, F.M.; Agterberg, F.P.; Ogg, J.G.; Petrizzo, M.R. The Cretaceous Period. In *Geologic Time Scale 2020*; Elsevier: Amsterdam, The Netherlands, 2020; Volume 2, pp. 1023–1086.
43. Jin, D.C.; Zhang, J.L.; Xu, X.; Jin, C.Z.; Jin, F.; Cai, Y.Y. A preliminary report on the Yanji dinosaur fauna in Jilin. *Acta Palaeontol. Sin.* **2018**, *57*, 495–503, (In Chinese with English Abstract).
44. Day, R.; Fuller, M.; Schmidt, V.A. Hysteresis properties of titanomagnetites: Grain-size and compositional dependence. *Phys. Earth Planet. Inter.* **1977**, *13*, 260–267. [CrossRef]
45. Robertson, D.J.; France, D.E. Discrimination of remanence-carrying minerals in mixtures, using isothermal remanent magnetisation acquisition curves. *Phys. Earth Planet. Inter.* **1994**, *82*, 223–234. [CrossRef]
46. Kruiver, P.P.; Dekkers, M.J.; Heslop, D. Quantification of magnetic coercivity components by the analysis of acquisition curves of isothermal remanent magnetisation. *Earth Planet. Sci. Lett.* **2001**, *189*, 269–276. [CrossRef]
47. Heslop, D.; Dekkers, M.J.; Kruiver, P.P.; Van Oorschot, I. Analysis of isothermal remanent magnetization acquisition curves using the expectation-maximization algorithm. *Geophys. J. Int.* **2002**, *148*, 58–64. [CrossRef]
48. Qin, H.F.; Zhao, X.M.; Liu, S.C.; Paterson, G.A.; Jiang, Z.X.; Cai, S.H.; Li, J.H.; Liu, Q.S.; Zhu, R.X. An ultra-low magnetic field thermal demagnetizer for high-precision paleomagnetism. *Earth Planets Space* **2020**, *72*, 1–12. [CrossRef]
49. Kirschvink, J.L. The least-squares line and plane and the analysis of palaeomagnetic data. *Geophys. J. Int.* **1980**, *62*, 699–718. [CrossRef]
50. Jones, C.H. User-driven integrated software lives: "Paleomag" paleomagnetics analysis on the Macintosh. *Comput. Geosci.* **2002**, *28*, 1145–1151. [CrossRef]
51. Sláma, J.; Košler, J.; Condon, D.J.; Crowley, J.L.; Gerdes, A.; Hanchar, J.M.; Horstwood, M.S.; Morris, G.A.; Nasdala, L.; Norberg, N. Plešovice zircon—A new natural reference material for U–Pb and Hf isotopic microanalysis. *Chem. Geol.* **2008**, *249*, 1–35. [CrossRef]
52. Li, X.H.; Liu, Y.; Li, Q.L.; Guo, C.H.; Chamberlain, K.R. Precise determination of Phanerozoic zircon Pb/Pb age by multicollector SIMS without external standardization. *Geochem. Geophys. Geosystems* **2009**, *10*, Q04010.
53. Li, X.H.; Tang, G.Q.; Gong, B.; Yang, Y.H.; Hou, K.J.; Hu, Z.C.; Li, Q.L.; Liu, Y.; Li, W.X. Qinghu zircon: A working reference for microbeam analysis of U-Pb age and Hf and O isotopes. *Chin. Sci. Bull.* **2013**, *58*, 4647–4654. [CrossRef]
54. Li, Q.L.; Li, X.H.; Liu, Y.; Tang, G.Q.; Yang, J.H.; Zhu, W.G. Precise U–Pb and Pb–Pb dating of Phanerozoic baddeleyite by SIMS with oxygen flooding technique. *J. Anal. At. Spectrom.* **2010**, *25*, 1107–1113. [CrossRef]
55. Stacey, J.S.; Kramers, J.D. Approximation of terrestrial lead isotope evolution by a two-stage model. *Earth Planet. Sci. Lett.* **1975**, *26*, 207–221. [CrossRef]
56. Ludwig, K.R. Isoplot 3.75: A Geochronological Toolkit for Microsoft Excel. *Berkeley CA Berkeley Geochronol. Cent. Spec. Publ.* **2012**, *5*, 1–75.
57. Deng, C.L.; Zhu, R.X.; Jackson, M.J.; Verosub, K.L.; Singer, M.J. Variability of the temperature-dependent susceptibility of the Holocene eolian deposits in the Chinese loess plateau: A pedogenesis indicator. *Phys. Chem. Earth Part A Solid Earth Geod.* **2001**, *26*, 873–878. [CrossRef]
58. Oches, E.A.; Banerjee, S.K. Rock-magnetic proxies of climate change from loess -paleosol sediments of the Czech Republic. *Stud. Geophys. Geod.* **1996**, *40*, 287–300. [CrossRef]
59. Roberts, A.P.; Pike, C.R.; Verosub, K.L. First-order reversal curve diagrams: A new tool for characterizing the magnetic properties of natural samples. *J. Geophys. Res. Solid Earth* **2000**, *105*, 28461–28475. [CrossRef]
60. Muxworthy, A.R.; Dunlop, D.J. First-order reversal curve (FORC) diagrams for pseudo-single-domain magnetites at high temperature. *Earth Planet. Sci. Lett.* **2002**, *203*, 369–382. [CrossRef]
61. Zijderveld, J.D.A. *Ac Demagnetization of Rocks: Analysis of Results*; Elsevier: New York, NY, USA, 1967; Volume 3, pp. 254–286.

62. Zhang, H.C. Early Cretaceous insects from the Dalazi Formation of the Zhixin Basin, Jilin Province, China. *Palaeoworld* **1997**, *7*, 75–103.
63. Li, X.H.; Liu, X.M.; Liu, Y.S.; Su, L.; Sun, W.D.; Huang, H.Q.; Yi, K. Accuracy of LA-ICPMS zircon U-Pb age determination: An inter-laboratory comparison. *Sci. China Earth Sci.* **2015**, *58*, 1722–1730. [CrossRef]
64. Ren, J.Y.; Tamaki, K.; Li, S.T.; Zhang, J.X. Late Mesozoic and Cenozoic rifting and its dynamic setting in Eastern China and adjacent areas. *Tectonophysics* **2002**, *344*, 175–205. [CrossRef]
65. Zhu, R.X.; Xu, Y.G. The subduction of the west Pacific plate and the destruction of the North China Craton. *Sci. China Earth Sci.* **2019**, *62*, 1340–1350. [CrossRef]
66. Wang, T.T.; Ramezani, J.; Wang, C.S.; Wu, H.C.; He, H.Y.; Bowring, S.A. High-precision U–Pb geochronologic constraints on the Late Cretaceous terrestrial cyclostratigraphy and geomagnetic polarity from the Songliao Basin, Northeast China. *Earth Planet. Sci. Lett.* **2016**, *446*, 37–44. [CrossRef]
67. Liu, S.; Gao, Y.F.; Yin, Y.K.; Liu, H.B.; Li, H.H.; Wang, P.J. Fine description and geological age delineation of sedimentary sequences of second member of Denlouku Formation based on ICDP scientific drilling borehole in Songliao Basin (SK2). *World Geol.* **2019**, *38*, 1032–1043, (In Chinese with English Abstract).
68. Zhang, F.Q.; Chen, H.L.; Yu, X.; Dong, C.W.; Yang, S.F.; Pang, Y.M.; Batt, G.E. Early Cretaceous volcanism in the northern Songliao Basin, NE China, and its geodynamic implication. *Gondwana Res.* **2011**, *19*, 163–176. [CrossRef]
69. Zhang, F.Q.; Dilek, Y.; Chen, H.L.; Yang, S.F.; Meng, Q.A. Structural architecture and stratigraphic record of Late Mesozoic sedimentary basins in NE China: Tectonic archives of the Late Cretaceous continental margin evolution in East Asia. *Earth-Sci. Rev.* **2017**, *171*, 598–620. [CrossRef]
70. Huang, Q.H.; Wu, H.C.; Wan, X.Q.; He, H.Y.; Deng, C.L. New progress of integrated chronostratigraphy of the Cretaceous in Songliao Basin. *J. Stratigr.* **2011**, *35*, 250–257, (In Chinese with English Abstract).
71. Zhang, S.; Fang, S.; Shao, H.J.; Wang, S.L.; Zhao, Y.; Ping, S.F. A New Zircon U–Pb Age of 107.15 Ma for the Dongshan Formation, Boli Basin, Northeast China. *Acta Geol. Sin.* **2020**, *94*, 568–571. [CrossRef]
72. Chen, D.X.; Zhang, F.Q.; Tian, Y.T.; Zhou, Z.H.; Dilek, Y. Timing of the late Jehol Biota: New geochronometric constraints from the Jixi Basin, NE China. *Palaeogeogr. Palaeoclim. Palaeoecol.* **2018**, *492*, 41–49. [CrossRef]
73. Zhao, L.; Gao, F.H.; Zhang, Y.L.; Xu, H.M.; Zhang, L.Y. Zircon U-Pb chronology and its geological implications of Mesozoic volcanic rocks from the Hailaer basin. *Acta Petrol. Sin.* **2013**, *29*, 864–874.
74. Wang, Y.Q.; Sha, J.G.; Pan, Y.H.; Zhang, X.L.; Rao, X. Non-marine Cretaceous ostracod assemblages in China: A preliminary review. *J. Stratigr.* **2012**, *36*, 289–299.
75. Zhang, L.J. Late Jurassic and early Cretaceous ostracod assemblages of Northeast China. *Sci. China Ser. B Chem. Biol. Agric. Med. Earth Sci.* **1988**, *31*, 1374–1386.
76. Wu, H.Y.; Huang, Q.H.; Dang, Y.M.; Kong, H.; Wang, L.Q. Achievements in the study on Cretaceous biostratigraphy of the Hailaer Basin, Inner Mongolia. *Acta Palaeontol. Sin.* **2006**, *45*, 283–291, (In Chinese with English Abstract).
77. Zhang, F.Q.; Chen, H.L.; Batt, G.E.; Dilek, Y.; Min-Na, A.; Sun, M.D.; Yang, S.F.; Meng, Q.A.; Zhao, X.Q. Detrital zircon U–Pb geochronology and stratigraphy of the Cretaceous Sanjiang Basin in NE China: Provenance record of an abrupt tectonic switch in the mode and nature of the NE Asian continental margin evolution. *Tectonophysics* **2015**, *665*, 58–78. [CrossRef]